ACS central science

http://pubs.acs.org/journal/acscii

Research Article

Atomically Dispersed Iridium on Indium Tin Oxide Efficiently Catalyzes Water Oxidation

Dmitry Lebedev, Roman Ezhov, Javier Heras-Domingo, Aleix Comas-Vives, Nicolas Kaeffer, Marc Willinger, Xavier Solans-Monfort,* Xing Huang,* Yulia Pushkar,* and Christophe Copéret*

Cite This: *ACS Cent. Sci.* 2020, 6, 1189–1198

Read Online

ACCESS | Metrics & More | Article Recommendations | Supporting Information

ABSTRACT: Heterogeneous catalysts in the form of atomically dispersed metals on a support provide the most efficient utilization of the active component, which is especially important for scarce and expensive late transition metals. These catalysts also enable unique opportunities to understand reaction pathways through detailed spectroscopic and computational studies. Here, we demonstrate that atomically dispersed iridium sites on indium tin oxide prepared via surface organometallic chemistry display exemplary catalytic activity in one of the most challenging electrochemical processes, the oxygen evolution reaction (OER). *In situ* X-ray absorption studies revealed the formation of Ir^{V}=O intermediate under OER conditions with an Ir−O distance of 1.83 Å. Modeling of the reaction mechanism indicates that Ir^{V}=O is likely a catalyst resting state, which is subsequently oxidized to Ir^{VI} enabling fast water nucleophilic attack and oxygen evolution. We anticipate that the applied strategy can be instrumental in preparing and studying a broad range of atomically dispersed transition metal catalysts on conductive oxides for (photo)electrochemical applications.

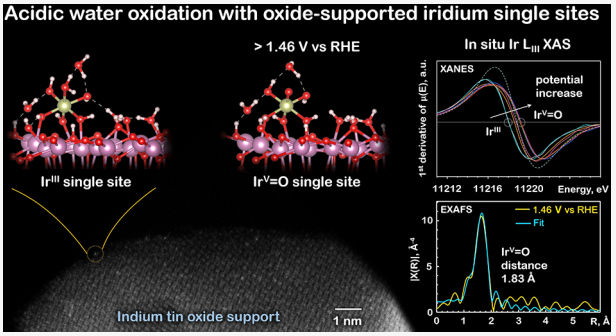

INTRODUCTION

Atomically dispersed late transition metals (often referred to as single-atom catalysts, SACs) enable numerous processes including alkene hydrogenation,[1] CO oxidation,[2−5] electro-[6−11] and photocatalysis,[12,13] etc. They represent an ultimate dispersion of a metal on a surface with all the atoms being exposed, which is critical for the expensive and scarce noble metal catalysts, such as Ir, Pd, and Pt. In addition, SACs open specific reaction pathways[12,14] and are well suited for a molecular-level understanding of the active-site structure and reaction mechanism by using a variety of element specific analytical tools, augmented by *in situ*/*operando* characterization coupled with computational modeling.[1,2,7,9]

Water splitting, widely considered the most sustainable method for hydrogen production, is perhaps one of the ultimate platforms for exploiting SACs.[15−20] Water splitting is most efficiently carried out in either acidic or alkali conditions and consists of two half-reactions: hydrogen and oxygen evolution reactions (HER and OER). Acidic water electrolysis offers a number of advantages over alkali water electrolysis including much larger operative current density and pressure,[21] yet it is strongly limited by the OER. A large overpotential and harsh reaction conditions of the OER in an acidic environment result in high catalyst instability, limiting the pool of possible candidates to solely iridium- and ruthenium-based materials, utilized mostly in the form of films or nanoparticles.

We reasoned that employing SAC for the acidic OER offers multiple opportunities and advantages over classical catalysts. First, ultimate catalyst dispersion allows decreasing the noble metal content in the catalyst, which is critical for the development of cost-effective acidic water electrolysis.[22] Second, studying OER SAC can help shed light on the reaction mechanism, which currently remains under debate due to its high complexity.[23−25] The proposed OER mechanisms differ by the nature of the O—O bond formation step: water nucleophilic attack (WNA) on a high-valent M=O intermediate versus radical coupling of two M=O intermediates.[26−28] The nature of SACs eliminates the radical coupling approach due to the physical separation of active sites on a support surface, and therefore, testing the catalytic activity of SAC in the OER and studying the reaction mechanism by *in situ* spectroscopy can potentially lead to observing reaction intermediates and the discovery of novel reaction pathways.

We thus generated isolated iridium sites on a conductive oxide support (indium tin oxide, ITO), which, to the best of our knowledge, is the first iridium SAC for the acidic OER. In

Received: May 12, 2020
Published: July 1, 2020

https://dx.doi.org/10.1021/acscentsci.0c00604
ACS Cent. Sci. 2020, 6, 1189−1198

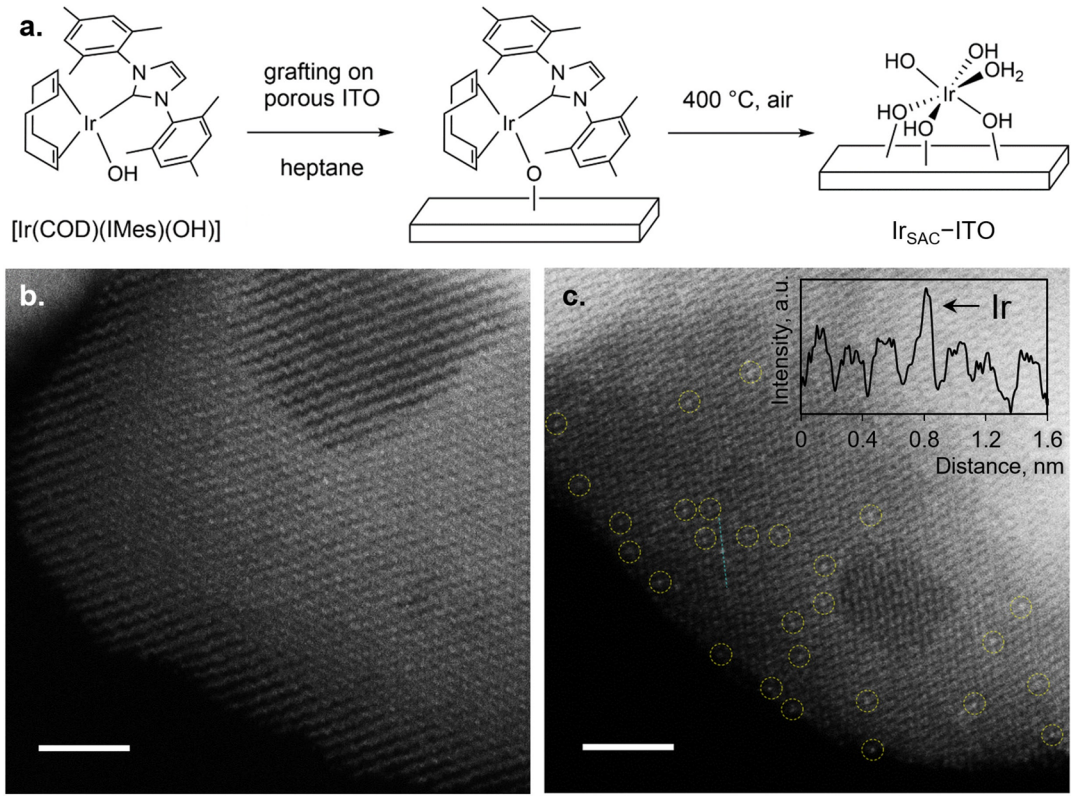

Figure 1. (a) Ir_{SAC}–ITO preparation scheme with the proposed structure of the surface site (after exposure to ambient conditions). HAADF-STEM images of [Ir(COD)(IMes)(OH)] grafted on ITO (b) and Ir_{SAC}–ITO (c); scale bars are 2 nm. Bright dots highlighted with yellow circles are assigned to isolated Ir atoms. Inset shows the line intensity profile over the single Ir atom on the ITO surface.

fact, previous studies of mononuclear and dinuclear Ir electrocatalysts were limited to neutral conditions due to the catalyst degradation in acid.[16] We further demonstrated that the activity of isolated Ir sites is on par with the state-of-the-art catalysts, which raises the question of reaction mechanism. We subsequently performed detailed electrochemical experiments coupled with *in situ* X-ray absorption spectroscopy that revealed the formation of a high-valent Ir^{V}=O intermediate, which so far remains elusive for the classical heterogeneous IrO_x catalysts.[29,30] Our DFT computational studies further support the formation of Ir^{V}=O as a resting state and its conversion into highly reactive Ir^{VI}=O, which generates O_2 upon reaction with water via the WNA mechanism. We also show that at higher current density isolated Ir sites can readily migrate to form small clusters that open additional OER reaction pathways.

RESULTS AND DISCUSSION

Generation and Characterization of Isolated Ir Sites.

Most of the reported single atom electrocatalysts are prepared on carbon-based supports,[8,20] which offers a number of advantages including high surface area and low support contrast in transmission electron microscopy. As these carbon-based supports are prone to degradation under harsh oxidizing OER conditions,[31] we decided to utilize a conductive oxide (ITO), which in addition to higher OER stability possesses surface hydroxyl groups allowing for controllable anchoring of molecular species.[32−35] Using surface organometallic chemistry (SOMC),[32−35] we grafted [Ir(COD)(IMes)(OH)] (COD = cyclooctadiene; IMes = 1,3-dimesitylimidazol-2-ylidene) on porous ITO electrodes and subsequently calcined the sample at 400 °C to remove all organic ligands, yielding Ir_{SAC}–ITO (Figure 1a).[35,36] We note that after the 400 °C calcination step the exact coordination environment of the Ir site is not fully known; therefore, the Ir_{SAC}–ITO structure depicted in Figure 1a reflects the proposed surface site after exposure to ambient conditions (e.g., moisture) and is in line with the computational model introduced below. High-angle annular dark-field scanning transmission electron microscopy (HAADF-STEM) studies of the grafted sample (Figure 1b and Figure S2) show only the presence of crystalline ITO without any sign of iridium deposition. After calcination, bright dots clearly appear on the ITO surface (highlighted in dotted yellow circles in Figure 1c; Figure S3), which we attribute to single iridium atoms.[16,17] Note that no Ir or IrO_2 clusters or nanoparticles are observed. The line profile across the bright dot highlights the increase of the intensity compared to the support which is due to strong scattering of Ir. The absence of bright dots on the grafted sample is likely due to the dangling of the surface grafted species over image accumulation time (smearing the HAADF-STEM intensity), whereas upon the calcination Ir strongly anchors to the ITO surface and becomes clearly visible in HAADF-STEM.

In order to further make evident the formation of isolated Ir atoms on the ITO surface, we performed Fourier filtering of the ITO lattice periodic contrast for the images of pristine ITO and Ir_{SAC}–ITO. While Fourier filtered ITO images show uniform gray contrast, nonperiodic white dots for Ir_{SAC}–ITO further support the formation of atomically dispersed Ir (Figure S4). We note that most likely the oxidative environment at an elevated temperature favors Ir dispersion

https://dx.doi.org/10.1021/acscentsci.0c00604
ACS Cent. Sci. 2020, 6, 1189−1198

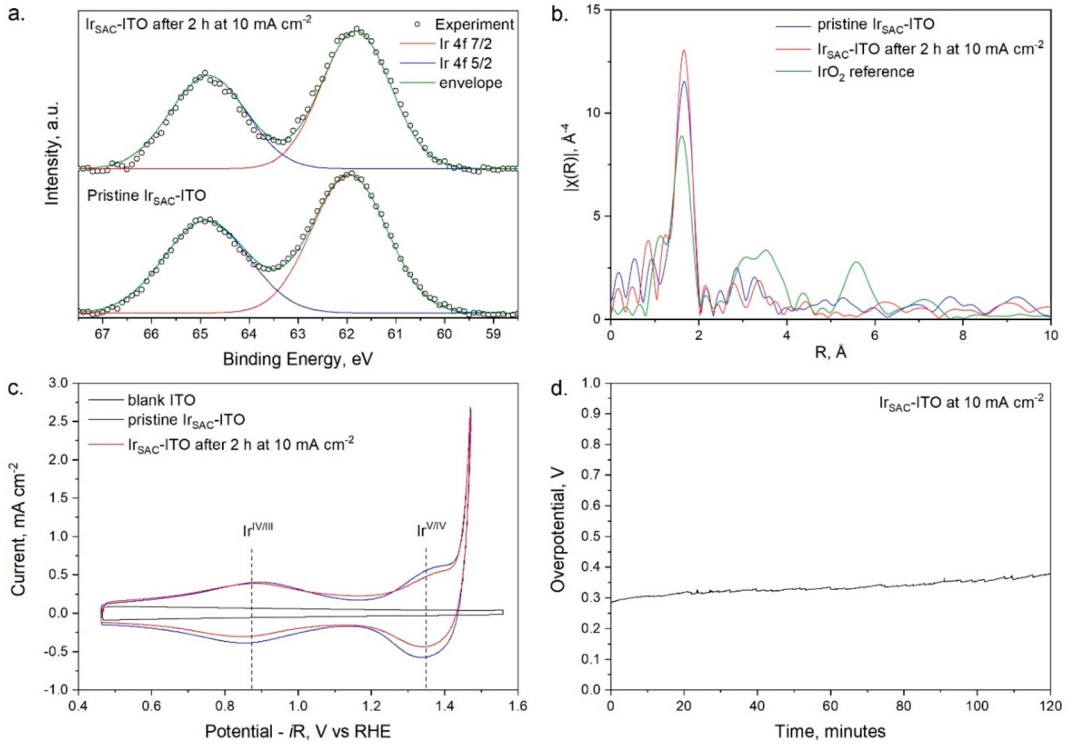

Figure 2. Spectroscopic and electrochemical characterization of Ir_{SAC}–ITO. Ir 4f XPS (a) and EXAFS (b) data of pristine Ir_{SAC}–ITO and Ir_{SAC}–ITO after 2 h at 10 mA cm^{-2} showing no change in the catalyst structure. (c) Cyclic voltammetry of blank ITO, pristine Ir_{SAC}–ITO, and Ir_{SAC}–ITO after 2 h at 10 mA cm^{-2} (0.1 M $HClO_4$, 10 mV s^{-1}) revealing $Ir^{IV/III}$ and $Ir^{V/IV}$ redox waves. (d) 2 h 10 mA cm^{-2} chronopotentiometric measurement of Ir_{SAC}–ITO showing high stability of the catalyst.

Table 1. Structural Parameters for Fits[a] of the *ex Situ* and *in Situ* EXAFS Data for Ir_{SAC}–ITO

sample	fit no.	shell	*R*, Å	*N*[b]	$\sigma^2 \times 10^3$	*R*-factor	reduced Chi^2
pristine Ir_{SAC}–ITO (*ex situ*); 3.2–10.68 k-space; 1.25–2.08 R-space	1[c]	Ir–O	2.04	6[c]	5.6	0.003	214
Ir_{SAC}–ITO after 2 h at 10 mA cm^{-2} (*ex situ*); 3.2–10.68 *k*-space; 1.25–2.08 *R*-space	2[c]	Ir–O	2.03	6[c]	5.1	0.002	376
Ir_{SAC}–ITO at 1.46 V vs RHE (*in situ*); 3.2–10.68 *k*-space; 1.25–2.04 *R*-space	3	Ir–O	2.00	6	4.9	0.004	240
Ir_{SAC}–ITO at 1.46 V vs RHE (*in situ*); 3.2–10.68 *k*-space; 1.25–2.04 *R*-space	4	Ir–O Ir–O	1.80 1.99	1 5	3.5[b] 3.5[b]	0.0006	40
Ir_{SAC}–ITO at 1.46 V vs RHE (*in situ*); 3.2–12.26 *k*-space; 1.25–2.04 *R*-space	5	Ir–O	2.01	6	7.0	0.005	40
Ir_{SAC}–ITO at 1.46 V vs RHE (*in situ*); 3.2–12.26 *k*-space; 1.25–2.04 *R*-space	6	Ir–O Ir–O	1.83 2.03	1 5	2.3[b] 2.3[b]	0.0013	11

[a]Fits were done in the *q*-space. *R* is the Ir–backscatter distance. σ^2 is the Debye–Waller factor. *R*-factor and reduced Chi^2 are the goodness-of-fit parameters. $S_0^2 = 1.0$ was used for all the fits. [b]Denotes that σ^2 was set to be the same for multiple vectors. [c]Note that changing the number of neighbors ($N = 5$ or 7) and/or splitting the first coordination shell did not improve these fits.

on the ITO surface, as grafting and calcination of multinuclear Ir compounds also lead to the formation of single atom species (Figure S5).

Elemental analysis of the Ir_{SAC}–ITO electrodes gives an Ir loading of 0.86 wt %, corresponding to the loading of 110 ± 10 nmol(Ir) cm$^{-2}_{electrode}$ (21 ± 2 μg(Ir) cm$^{-2}_{electrode}$, 0.62 ± 0.06 Ir nm$^{-2}_{ITO}$), which is significantly lower compared to the loadings typically used for OER catalysts.[37,38] Visible–near-IR transmission studies of the electrodes (Figure S17) show that deposition of iridium does not lead to a significant increase of light absorption at the electrodes (on average 4% decrease of the transmission), which is in line with the low iridium loading and atomic nature of the iridium species. The proposed catalyst design is thus suitable as a transparent OER electrocatalytic layer for use in the sunlight-driven water splitting devices.

XPS studies of the Ir_{SAC}–ITO (Figure S18) show the presence of O, In, Sn, and Ir, consistent with the sample composition. The Ir 4f region (Figure 2a) consists of two peaks, which are assigned to the spin–orbit split Ir 4f components: Ir 4f 7/2 and Ir 4f 5/2. We find the Ir 4f 7/2 energy of 61.9 eV, which corresponds to Ir^{III}.[9] While XPS spectra of conductive Ir-containing compounds (Ir metal, IrO_2, Ir pyrochlores, etc.) always display asymmetrical line shapes

https://dx.doi.org/10.1021/acscentsci.0c00604
ACS Cent. Sci. 2020, 6, 1189–1198

(originating from the electron screening effects),[39−41] Ir 4f peaks of Ir_{SAC}−ITO are symmetrical and therefore were fitted using a Gaussian line shape. The symmetrical line shape arises from the absence of the electron screening effects and is consistent with the absence of the iridium (oxide) bulk metallic character, further supporting the presence of isolated Ir sites.

In order to further probe the Ir oxidation state and coordination environment, we performed *ex situ* and *in situ* (*vide infra*) X-ray absorption spectroscopy (XAS) studies at the Ir L_{III} edge (see details in the SI). X-ray absorption near-edge spectra (XANES, Figure S19) yielded an Ir edge energy (defined here as a maximum of the white line) of 11218 eV consistent with Ir^{III}.[38,39] Extended X-ray absorption fine structure (EXAFS) data in the *R*-space (Figure 2b) have one major peak at approximately 2 Å, which corresponds to the first coordination shell of iridium (Ir−O). Minor peaks at ∼2.5−3.5 Å apparent distance likely originate from the contribution of the ITO support. The lack of strong Ir−Ir or Ir−O−Ir interactions expected at ∼2.7 or ∼3.5 and ∼5.5 Å apparent distance, respectively, infers the absence of large iridium and iridium oxide aggregates (Figure 2b). We find that the best model for the first coordination sphere of Ir is 6 oxygen neighbors at a distance of 2.04 ± 0.02 Å (see Table 1 and Figure S20), which is very close to 2.03 ± 0.01 Å found for Ir^{III} in IrO_x.[39] Note that either changing the number of neighbors (N = 5 or 7) or splitting the first coordination shell does not improve the fit (results in larger Chi^2).

Electrochemical Studies and OER Activity. Electrochemical studies of Ir_{SAC}−ITO were performed in 0.1 M $HClO_4$ electrolyte (pH 1) with the additional cyclic voltammetry measurements at pH 4. Cyclic voltammetry (Figure 2c and Figure S11) at pH 1 shows the presence of two redox waves located at 0.89 and 1.35 V vs the reversible hydrogen electrode (RHE), assigned to $Ir^{IV/III}$ and $Ir^{V/IV}$ transitions, respectively,[42] followed by an increase in current corresponding to catalytic water oxidation. Measurements at pH 4 (Figure S12) produce the same shape voltammogram with redox waves located at 0.85 and 1.37 V vs RHE. These values are very close to those obtained at pH 1, which indicates that both $Ir^{IV/III}$ and $Ir^{V/IV}$ redox transitions are proton coupled electron transfer (PCET) steps. The linear dependence of the $Ir^{IV/III}$ peak current (pH 1, forward scan) with the scan rate indicates that the redox event is associated with the electrode-bound species (Figure S13). Integration of the $Ir^{IV/III}$ couple results in electroactive Ir loading of 100 ± 10 nmol(Ir) cm^{-2}, which is in a good agreement with the loading of 110 ± 10 nmol(Ir) cm^{-2} obtained from the elemental analysis. The fact that most of the capacitive response from the voltammograms of Ir_{SAC}−ITO originates from the ITO support and not from Ir (which only contributes to the redox events and OER catalytic current, contrary to the CV studies of iridium nanoparticles on ITO)[37] confirms the high dispersion of the electroactive species for Ir_{SAC}−ITO.

The OER catalytic activity of Ir_{SAC}−ITO was examined using linear sweep voltammetry (Figure S16a), steady-state chronoamperometric, and chronopotentiometric measurements in 0.1 M $HClO_4$. Using a Clark oxygen sensor, we show that Ir_{SAC}−ITO produces O_2 with 99% Faradaic efficiency (H_2O_2 yield <1%, see Figure S15 and details in the SI). The slope of the Ir_{SAC}−ITO Tafel plot (Figure S16b) is 46 ± 4 mV dec^{-1}, similar to what is observed on iridium oxide nanoparticles[39,42,43] and significantly smaller than 66−118 mV dec^{-1} reported for molecular Ir catalyst deposited on ITO.[44] The current density of 10 A g_{Ir}^{-1} is reached at an overpotential of 220 ± 5 mV, which is lower than 240 mV reported for Ir nanoparticles dispersed on ITO[37] and high surface area IrO_2 and IrO_2−TiO_2 catalysts (260−270 mV).[39,45] Ir_{SAC}−ITO produces the current density of 49 ± 5 A $g(Ir)^{-1}$ and 156 ± 13 A $g(Ir)^{-1}$ at 1.48 and 1.51 V vs RHE respectively, which is higher than values reported for state-of-the-art Ir and IrO_2 catalysts[42,46] and approaches the highest performing mixed metal Ir−M catalysts (see Table S1 for a detailed comparison).[47,48] The high activity of the Ir_{SAC}−ITO is likely due to the ultimate Ir dispersion on the electrode surface and hence optimal utilization of Ir. These results demonstrate that isolated Ir surface sites can reach high catalytic turnover in the 4-electron water oxidation without the need of adjacent Ir partners or underlying Ir/IrO_x bulk (*vide infra*).

The stability of Ir_{SAC}−ITO was investigated by carrying out a 3 h electrolysis test at 0.5 mA cm^{-2} (Figure S14) and a 2 h electrolysis test at 10 mA cm^{-2} (Figure 2d),[24] which corresponds to turnover numbers (TONs) of approximately 130 and 1700 O_2 molecules per Ir atom, respectively (see details in the SI). During these experiments, the Ir_{SAC}−ITO catalyst shows nearly no drift in potential and requires on average 255 ± 10 and 350 ± 20 mV overpotential to drive the current of 0.5 and 10 mA cm^{-2}, respectively. A similar overpotential of 340 ± 20 mV at 10 mA cm^{-2} is found for Ir nanoparticles dispersed on ITO[37] at the expense of a 5 times higher Ir loading.

The use of electrodes with relatively high surface area (hence large amount of catalyst) allows for postanalyses of the catalyst and, more importantly, *in situ* studies (*vide infra*).[37] We find that both Ir 4f XPS and XAS data of Ir_{SAC}−ITO after 2 h electrolysis at 10 mA cm^{-2} (Figure 2 and Figure S19) are nearly identical to the data of the pristine sample, indicating that the Ir oxidation state relaxes to the original Ir^{III}; there are no changes in the Ir local coordination environment and no formation of large Ir or IrO_2 nanoparticles. However, knowing that XPS and XAS analyses are not sensitive to formation of ultrasmall clusters, we performed detailed HAADF-STEM characterization of Ir_{SAC}−ITO at different stages of our electrochemical tests. HAADF-STEM images of Ir_{SAC}−ITO recorded after just immersing the electrode in the electrolyte for 5 min, after 10 CV cycles from 0.46 to 1.56 V vs RHE (25 mV s^{-1}), and after a representative activity test (chronoamperometry from 1.41 to 1.53 V vs RHE with 25 mV steps in 0.1 M $HClO_4$) show no difference compared to the pristine Ir_{SAC}−ITO (Figures S6−S8). However, HAADF-STEM images of Ir_{SAC}−ITO after 3 h at 0.5 mA cm^{-2} show that part of iridium single sites aggregated into small clusters, with the effect being more pronounced after 2 h electrolysis at 10 mA cm^{-2} (Figures S9−S10). Formation of these aggregates with a diameter of approximately 0.6 nm indicates mobility of the surface Ir species during prolonged OER tests at high potentials. Cyclic voltammetry studies of Ir_{SAC}−ITO after 2 h electrolysis at 10 mA cm^{-2} (Figure S14) show no change of Ir loading, which excludes Ir leaching in the electrolyte. Broadening of the CV redox waves indicates the presence of the distribution of surface Ir species, most probably associated with the coexistence of Ir single sites and aggregates of different sizes as revealed by HAADF-STEM. The Ir mobility on the ITO surface under OER conditions may be explained by ITO surface reconstruction under applied potential or the

https://dx.doi.org/10.1021/acscentsci.0c00604
ACS Cent. Sci. 2020, 6, 1189−1198

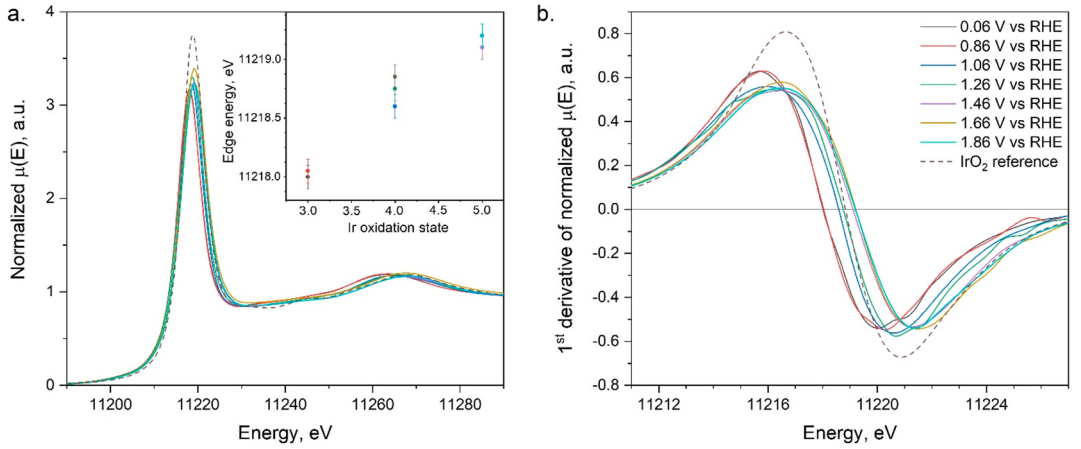

Figure 3. *In situ* studies of Ir_{SAC}–ITO. Ir L_{III}-edge XANES spectra (a) and their first derivatives (b) reveal the shift of the edge energy as a function of the applied potential. Inset shows assignment of the edge energy to a certain Ir oxidation state.

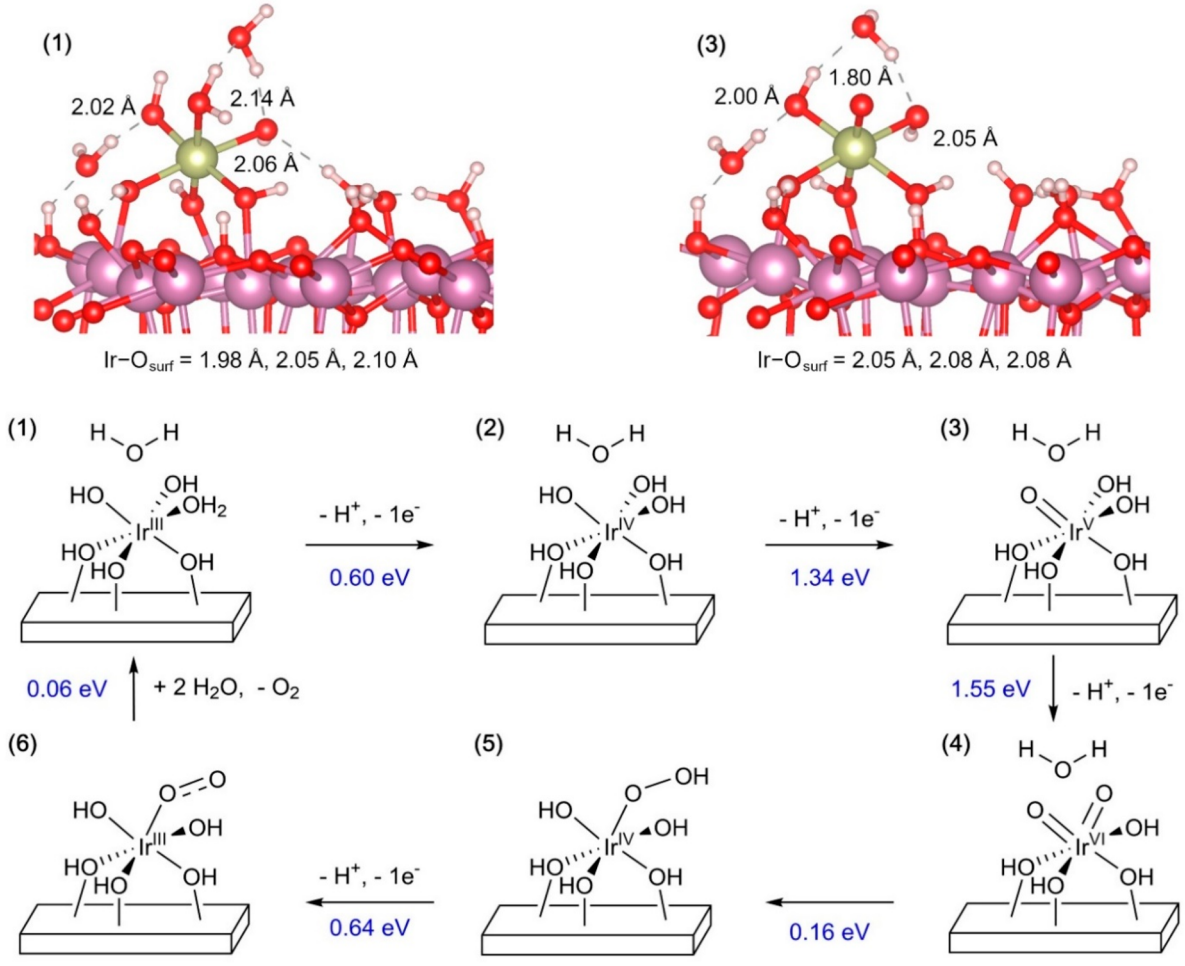

Figure 4. Computed OER mechanism with the structures of Ir_{SAC}–ITO (**1**) and Ir^{V}=O site (**3**) shown on top. The mechanism involves the PCET step of observed Ir^{V}=O to proposed Ir^{VI}=O followed by WNA.

involvement of surface indium or tin atoms in the OER process, although the exact origin and mechanism of Ir mobility and aggregation remain unclear. Whether the Ir clustering leads to the decrease in OER performance and is responsible for the slight increase of the potential required to maintain the 10 mA cm^{-2} current (Figure 2d), or other degradation pathways play a role, requires further detailed studies.

EXAFS of spent electrodes shows a similar spectrum to the starting Ir_{SAC}–ITO, with a small contribution from the second coordination shell as for the starting material (Figure S20). This observation is in line with previous studies where no Ir–Ir contribution was detected for an Ir dimer deposited on

https://dx.doi.org/10.1021/acscentsci.0c00604
ACS Cent. Sci. 2020, 6, 1189–1198

Fe_2O_3.[16] The absence of scattering from the second coordination shell can be explained by the small size and disordered nature of the Ir clusters, which results in the distribution of Ir−Ir distances. Fitting the first coordination shell using the same model as for the initial electrode results in the Ir−O distance of 2.03 ± 0.02 Å, similar to the value obtained for the pristine Ir_{SAC}−ITO (Table 1).

***In Situ* XAS.** In order to investigate the iridium oxidation state and probe the coordination environment under OER conditions, we exploited *in situ* XAS studies at the Ir L_{III}-edge using a custom-designed electrochemical cell. The XANES spectra (Figure 3) show an increase of the edge energy with an increase of the applied potential (see Table 1). Based on the reference IrO_2 (Ir^{IV}), the oxidation states of the Ir were assigned to Ir^{III} (0−0.9 V vs RHE), Ir^{IV} (0.9−1.35 V vs RHE), and Ir^{V} (above 1.35 V vs RHE), which corroborates the assignment done from the electrochemical studies (Figure 2c). Similar shifts in the position of the Ir L_{III}-edge were reported in the XAS studies of the submonolayer film of IrO_x on RuO_2, although unknown catalyst morphology and structure did not allow correlating the observed changes with the changes of the local Ir coordination environment.[30] Moreover it is unclear whether the spectroscopic changes are associated with catalysis, as the submonolayer IrO_x film is grown on highly OER active RuO_2.

Performing *in situ* studies on single atom catalysts on an OER inactive support allows the overcoming of these limitations and controversy by reducing the complexity of the system. This approach enables establishing the local coordination environment of Ir and drawing of correlations with the catalyst OER activity. We collected *in situ* EXAFS data in the OER regime at a potential of 1.46 V vs RHE and a current of approximately 0.2 mA cm^{-2} (Figures S21 and S22). Attempts to collect EXAFS data at higher potentials were unsuccessful because of intense bubble formation due to the OER. Fitting the first iridium coordination shell using the same model as for the initial electrode (Figure S21 and fits 3 and 5 of Table 1) results in the Ir—O distance of 2.00 ± 0.02 Å, which is shorter than the distance obtained for pristine Ir_{SAC}−ITO. We found that splitting the first coordination shell into 5 + 1 oxygen scatterers (Figure S21 and fits 4 and 6 of Table 1) improves the fit quality (lower *R*-factor and reduced Chi^2) and results in the short Ir—O backscatterer at 1.83 ± 0.02 Å. We assign this short oxygen backscatterer to the Ir^{V}═O intermediate, which can be a predominant species for Ir_{SAC}−ITO under OER conditions (i.e., resting state of the catalyst).[27] For comparison, the only known terminal-oxo Ir^{V} complex (oxotrimesityliridium),[49] albeit in tetrahedral geometry, features a shorter Ir═O distance of 1.73 Å.

DFT Calculations under Periodic Boundary Conditions. After establishing that OER activity of the site-isolated Ir on ITO is on par with the state-of-the-art Ir catalysts, we carried out DFT periodic calculations with the VASP package (see the Methods section and the SI for the computational details) with the aim of gaining a further understanding of the catalytic cycle. Ir_{SAC}−ITO was modeled as a tris-bound Ir^{III} isomer of a general formula of $(\equiv In—\mu^2—OH)_3Ir(OH)_2(H_2O)$, where $(\equiv In—\mu^2—OH)$ describes bridging hydroxyl ligands bonded to Ir and In atoms of the oxide surface (Figure 4). The Ir—O distances vary from 1.98 to 2.14 Å with an average value of 2.06 Å (Table S2), which is close to 2.04 Å obtained via EXAFS modeling of the pristine Ir_{SAC}−ITO (Table 1). The first PCET oxidation to produce Ir^{IV} is calculated to occur at 0.60 V vs RHE followed by subsequent PCET oxidations to Ir^{V} and Ir^{VI} at 1.34 and 1.55 V vs RHE, respectively. While the Ir^{IV} intermediate (**2**, Figure S24) features three hydroxo groups, Ir^{V} species (Figure 4) bear an oxo group (Ir═O) at 1.80 Å, a distance that closely matches the experimental *in situ* EXAFS data recorded at 1.46 V vs RHE (1.83 Å for fit 6 of Table 1).

Next, we explored two possible pathways for O—O bond formation: direct WNA on pentavalent oxo complex (**3**) and on high-valent Ir^{VI} dioxo intermediate (**4**). While the WNA step directly from the pentavalent complex (**3**) is highly endergonic (0.97 eV, 22.4 kcal mol^{-1}, see Figure S26), we find very feasible energetics for the second pathway (Figure 4). Indeed, the PCET to form Ir^{VI} dioxo intermediate (**4**) can happen at 1.55 V vs RHE followed by a much less endergonic WNA step (0.16 eV, 3.7 kcal mol^{-1}) to form a hydroperoxo intermediate (**5**, Figure S24), with the subsequent steps requiring lower potentials. In summary, the latter pathway does not imply any challenging chemical steps and predicts an overpotential of 0.32 V, in agreement with the low overpotential observed experimentally. The fact that the Ir^{VI} intermediate is not observed in the experiment neither by electrochemistry nor by spectroscopy suggests that Ir^{V} is the resting state of the catalyst and that the Ir^{VI} species are short-lived. In this context, DFT calculations indicate that the WNA is too challenging on the site-isolated Ir^{V} species, and another PCET step is required to make the experimentally observed surface Ir^{V}═O more electrophilic. Interestingly, recent computational studies on molecular Ir complexes[50,51] found that formation of the high-valent Ir^{VI} intermediates is plausible in the experiments and facilitates the OER catalysis.[47] It is also worth noting that such proposed Ir^{VI} intermediates are isoelectronic to Ru^{V} species, which are proposed to play important role in molecular OER catalysts.[27,52−54]

As partial aggregation of Ir was observed during prolonged electrochemical stability tests, we decided to perform cluster calculations on Ir dimeric species in order to access the redox potentials. We find that the potentials required for oxidizing the Ir(III)−Ir(III) species to Ir(V)−Ir(V) are not consistent with the experimental CV and *in situ* XAS data (Figure S27), suggesting that iridium dimers are highly unlikely present in the initial material. However, if formed during the catalytic process as a consequence of Ir migration on the surface, our calculations suggest that the dimeric species would also be active at reaction conditions (see further details in the SI).

■ CONCLUSIONS

We have described the synthesis and characterization of an atomically dispersed Ir OER electrocatalyst, highly active and stable in acidic conditions. High-resolution electron microscopy images, a unique symmetrical Ir 4f XPS line shape, and clear redox transitions detected both electrochemically and by *in situ* XANES make evident the formation of isolated Ir^{III} sites on ITO. The OER activity of the catalyst ranks among those of the highest performing Ir and IrO_x catalysts, which is achieved due to the ultimate Ir dispersion and demonstrates that site-isolated mononuclear Ir centers can effectively catalyze the OER. *In situ* EXAFS studies of the catalyst during the OER reveal the presence of Ir^{V}═O species with the Ir—O distance of 1.83 Å. Computational modeling of the reaction pathway with isolated Ir sites indicates that the Ir^{V}═O species are the catalyst resting state that can further undergo a PCET step to form an Ir^{VI} dioxo intermediate, from which WNA is

https://dx.doi.org/10.1021/acscentsci.0c00604
ACS Cent. Sci. 2020, 6, 1189−1198

endergonic by only 0.16 eV. The feasible WNA step suggests that the Ir^{VI} dioxo species are short-lived under electrocatalytic conditions, explaining why they are not experimentally detected. While the catalyst stays in the atomically dispersed form during CV and chronoamperometry tests, high-resolution electron microscopy studies indicate that part of the iridium single sites aggregates in small clusters on a longer time scale under high applied potential. The mechanism of this process as well as its impact on the catalyst activity remain unclear and require future investigations.

Our studies show that surface organometallic chemistry is a powerful approach to access atomically dispersed and efficient metal sites on oxide supports enabling detailed characterization and mechanistic studies via state-of-the-art spectroscopic tools and computational modeling. This approach is likely general and applicable to a broad range of heterogeneous transformations including partial oxidation of methane, electroreduction of CO_2, (photo)electrochemical water splitting, etc.

METHODS

Ir_{SAC}–ITO Preparation. Grafting of [Ir(COD)(IMes)(OH)][55] on porous ITO electrodes[27,56] was performed under inert conditions according to the following procedure: 10 mg of [Ir(COD)(IMes)(OH)] were dissolved in 8 mL of dry, air-free heptane, and the obtained 2 mM solution was added to 10 porous ITO electrodes (1.5 cm^2 of ITO each) in the Petri dish in the glovebox. The Petri dish was sealed with parafilm to avoid heptane evaporation and left overnight. The electrodes were washed three times with heptane, calcined at 400 °C for 1 h (with the ramp of 60 °C h^{-1}), and exposed to ambient conditions to produce Ir_{SAC}–ITO. No unexpected or unusually high safety hazards were encountered.

General. High-angle annular dark-field scanning transmission electron microscopy (HAADF-STEM) imaging was performed using aberration-corrected JEOL JEM-ARM 200F and JEM-ARM 300F Grand ARM transmission electron microscopes operated at 200 and 300 kV, respectively. TEM samples were prepared by scratching ITO with surface Ir species from the fluorine doped tin oxide (FTO) surface followed by the dry deposition of the obtained powder on the Cu TEM grid (200 mesh) covered with the ultrathin holey carbon layer. After shaking off the material that is loosely attached to the carbon support, we mounted the grid into a standard single-tilt TEM sample holder. Fourier filtered images (Figure S4) were obtained by masking the periodic component in the FT image followed by an inverse FT. X-ray photoelectron spectroscopy (XPS) was conducted on an XPS Sigma 2 instrument (ThermoFisher Scientific, Loughborough, Great Britain) equipped with a UHV chamber (pressure < 10^{-6} Pa), a non-monochromatic 200 W Al Kα source, a hemispherical analyzer, and a seven channel electron multiplier. The analyzer-to-source angle is 50°, while the emission angle is 0°. A pass energy of 50 and 25 eV was set for the survey and the narrow scans, respectively. XPS data were analyzed in CasaXPS Version 2.3.19PR1.0 software; the binding energies of the acquired spectra were referenced to the C 1s line at 284.8 eV. Background subtraction was performed according to Shirley[57] (Shirley background modified with linear to capture the rising In 4p line at approximately 80 eV). Elemental analysis was performed by the Mikroanalytisches Labor Pascher, Remagen, Germany, using inductively coupled plasma (ICP)-based methods.

Electrochemical Characterization. Electrochemical measurements were performed in a standard single-compartment 3-electrode cell with Pt counter and Ag/AgCl reference electrodes. The porous ITO electrodes were electrically contacted using the uncoated FTO layer and masked to a geometrical surface area of 0.8–1.2 cm^2 using nonconductive epoxy (see Figure S12). 0.1 M $HClO_4$ or 0.1 M acetate buffer (with total ionic strength adjusted to 0.5 M with $NaClO_4$) was used as the electrolyte and was saturated with Ar prior to the measurements. Polarization curves were obtained in 0.1 M $HClO_4$ from the steady-state chronoamperometric measurements: the potential was gradually stepped from 1.41 to 1.53 V vs RHE (with 25 mV steps) while holding for 1 min at each potential. Electrochemical impedance spectroscopy measurements were used for Ohmic drop compensation. Chronopotentiometry (stability) measurements were performed in 0.1 M $HClO_4$ at 0.5 or 10 mA cm^{-2} for 3 or 2 h, respectively. Both vigorous stirring and argon bubbling of electrolyte were used for chronoamperometric and chronopotentiometric measurements. The current expressed as [mA cm^{-2}] refers to the geometrical surface area of the electrode, and [A g_{Ir}^{-1}] refers to the total mass of Ir on the electrode, determined using the elemental analysis. All reported measurements were repeated several times to ensure the reproducibility of the results. Unless specified otherwise, all the potential values are reported vs reversible hydrogen electrode (RHE) scale. See the SI for more details and the description of the Faraday efficiency measurement.

X-ray Absorption (XAS) Studies. XAS studies were performed at the Advanced Photon Source (APS) at Argonne National Laboratory in the fluorescence mode. *Ex situ* XAS was taken for reference IrO_2, pristine Ir_{SAC}–ITO, and Ir_{SAC}–ITO after 2 h of electrolysis at 10 mA cm^{-2} in 0.1 M $HClO_4$ (Figures S18 and S19). An electrochemical cell (10 mL) of custom design equipped with Ag/AgCl reference and Pt counter electrodes was used for the *in situ* measurements. All data were background-corrected, normalized, and deglitched (if necessary) and then converted to wave vector space (k-space) and weighted by k^3. k-space data were truncated near zero crossings before Fourier transformation. See more details in the SI. EXAFS data were analyzed using the Athena software package.[58]

Density Functional Theory (DFT). Geometry optimizations were carried out using spin-polarized PBE-D2[59,60] calculations as implemented in VASP code.[61,62] We considered the projector augmented wave (PAW) pseudopotentials and expanded the valence electrons in plane waves with a kinetic energy cutoff of 500 eV. The Brillouin zone was sampled with a Monkhorst-Pack grid of (6, 6, 6) and (6, 6, 1) k-points for bulk and slab calculations, respectively. The isolated Ir centers on ITO were represented with a 4-layer slab model of the (111) surface containing the Ir center coordinated to indium oxide support via three Ir–O(H)–In bonds. Water molecules were included around the active site to represent a high local water coverage. The c value was set to 35 Å ensuring an interlayer distance of at least 21 Å. Tin atoms were omitted in the calculation for simplification as we do not expect that the presence of very few Sn in the model would influence the electronic structure of Ir. The electronic energies for the OER mechanism were corrected with single point calculations applying an ONIOM like scheme[63] with two layers: (i) the low level corresponds to the PBE-D2 periodic model computed with VASP, and (ii) the inner layer corresponds

https://dx.doi.org/10.1021/acscentsci.0c00604
ACS Cent. Sci. 2020, 6, 1189–1198

to the $(H_2O)(OH)Ir(OH)_2(H_2O)$ cluster (for the initial Ir^{III} species). This inner part was computed with the highly accurate double-hybrid functional B2GP-PLYP[64] as implemented in ORCA.[65] In the molecular calculation, atoms were represented with the split-valence triple-z basis set with polarization def2-TZVP.[66] See the SI for more computational details.

■ ASSOCIATED CONTENT

Supporting Information

The Supporting Information is available free of charge at https://pubs.acs.org/doi/10.1021/acscentsci.0c00604.

Additional data, methods, and supplementary figures including HRTEM images, electrochemical and spectroscopic data, and details of the computational modeling (PDF)

■ AUTHOR INFORMATION

Corresponding Authors

Xavier Solans-Monfort − *Departament de Química, Universitat Autònoma de Barcelona, Bellaterra 08193, Catalonia, Spain;* orcid.org/0000-0002-2172-3895; Email: xavier.solans@uab.cat

Xing Huang − *Department of Chemistry and Applied Biosciences and Scientific Center for Optical and Electron Microscopy (ScopeM), ETH Zurich, CH-8093 Zurich, Switzerland;* orcid.org/0000-0002-8700-0606; Email: xing.huang@scopem.ethz.ch

Yulia Pushkar − *Department of Physics and Astronomy, Purdue University, West Lafayette, Indiana 47907, United States;* orcid.org/0000-0001-7949-6472; Email: ypushkar@purdue.edu

Christophe Copéret − *Department of Chemistry and Applied Biosciences, ETH Zurich, CH-8093 Zurich, Switzerland;* orcid.org/0000-0001-9660-3890; Email: ccoperet@ethz.ch

Authors

Dmitry Lebedev − *Department of Chemistry and Applied Biosciences, ETH Zurich, CH-8093 Zurich, Switzerland;* orcid.org/0000-0002-1866-9234

Roman Ezhov − *Department of Physics and Astronomy, Purdue University, West Lafayette, Indiana 47907, United States*

Javier Heras-Domingo − *Departament de Química, Universitat Autònoma de Barcelona, Bellaterra 08193, Catalonia, Spain*

Aleix Comas-Vives − *Departament de Química, Universitat Autònoma de Barcelona, Bellaterra 08193, Catalonia, Spain*

Nicolas Kaeffer − *Department of Chemistry and Applied Biosciences, ETH Zurich, CH-8093 Zurich, Switzerland*

Marc Willinger − *Scientific Center for Optical and Electron Microscopy (ScopeM), ETH Zurich, CH-8093 Zurich, Switzerland;* orcid.org/0000-0002-9996-7953

Complete contact information is available at: https://pubs.acs.org/10.1021/acscentsci.0c00604

Author Contributions

D.L. and C.C. conceived the project. C.C., M.W., X.S.-M., and Y.P. supervised the research. D.L. performed the preparation and characterization of samples as well as the electrochemical experiments with the help of N.K. R.E. and Y.P. performed *in situ* XAS studies and XAS data processing. X.H. performed microscopy measurements and J.H.-D., A.C.-V., and X.S.-M. performed the computational studies. All the authors interpreted the data and wrote the manuscript.

Funding

This research is based upon work supported by InnoSuisse through the Swiss Competence Center for Energy Research (SCCER) Heat & Electricity Storage and by the National Science Foundation, Division of Chemistry CHE-1900476 (Y.P.). The use of the Advanced Photon Source, an Office of Science User Facility operated by the U.S. Department of Energy (DOE) Office of Science by Argonne National Laboratory, was supported by the U.S. DOE under Contract DE-AC02-06CH11357. The PNC/XSD (Sector 20) facilities at the Advanced Photon Source and research at these facilities were supported by the U.S. Department of Energy—Basic Energy Science, the Canadian Light Source and its funding partners, the University of Washington, and the Advanced Photon Source. J. H.-D. and X.S.-M. acknowledge financial support from MINECO (CTQ2017-89132-P) and Generalitat de Catalunya (2017SGR1320). A.C.-V. acknowledges the financial support from the "Ramon y Cajal" Fellowship, funded by Spanish MEC and the European Social Fund (RyC-2016-19930) and and the Spanish "Ministerio de Ciencia, Innovación y Universidades" (PGC2018-100818-A-I00).

Notes

The authors declare no competing financial interest.

■ ACKNOWLEDGMENTS

X.H. and M.W. acknowledge Prof. Robert Schlögl from the Department of Inorganic Chemistry, Fritz Haber Institute of Max Plank Society for the use of JEOL JEM-ARM 200F TEM. We would like to acknowledge Athanasia Tsoukalou (ETH Zurich) for performing the XPS measurements.

■ REFERENCES

(1) Liu, P.; Zhao, Y.; Qin, R.; Mo, S.; Chen, G.; Gu, L.; Chevrier, D. M.; Zhang, P.; Guo, Q.; Zang, D.; Wu, B.; Fu, G.; Zheng, N. Photochemical route for synthesizing atomically dispersed palladium catalysts. *Science* **2016**, *352* (6287), 797−801.

(2) Qiao, B.; Wang, A.; Yang, X.; Allard, L. F.; Jiang, Z.; Cui, Y.; Liu, J.; Li, J.; Zhang, T. Single-atom catalysis of CO oxidation using Pt_1/FeO_x. *Nat. Chem.* **2011**, *3* (8), 634−641.

(3) Peterson, E. J.; DeLaRiva, A. T.; Lin, S.; Johnson, R. S.; Guo, H.; Miller, J. T.; Hun Kwak, J.; Peden, C. H.; Kiefer, B.; Allard, L. F.; Ribeiro, F. H.; Datye, A. K. Low-temperature carbon monoxide oxidation catalysed by regenerable atomically dispersed palladium on alumina. *Nat. Commun.* **2014**, *5*, 4885.

(4) DeRita, L.; Resasco, J.; Dai, S.; Boubnov, A.; Thang, H. V.; Hoffman, A. S.; Ro, I.; Graham, G. W.; Bare, S. R.; Pacchioni, G.; Pan, X.; Christopher, P. Structural evolution of atomically dispersed Pt catalysts dictates reactivity. *Nat. Mater.* **2019**, *18* (7), 746−751.

(5) Yoo, M.; Yu, Y.-S.; Ha, H.; Lee, S.; Choi, J.-S.; Oh, S.; Kang, E.; Choi, H.; An, H.; Lee, K.-S.; Park, J. Y.; Celestre, R.; Marcus, M. A.; Nowrouzi, K.; Taube, D.; Shapiro, D. A.; Jung, W.; Kim, C.; Kim, H. Y. A tailored oxide interface creates dense Pt single-atom catalysts with high catalytic activity. *Energy Environ. Sci.* **2020**, *13* (4), 1231−1239.

(6) Liu, D.; Li, X.; Chen, S.; Yan, H.; Wang, C.; Wu, C.; Haleem, Y. A.; Duan, S.; Lu, J.; Ge, B.; Ajayan, P. M.; Luo, Y.; Jiang, J.; Song, L. Atomically dispersed platinum supported on curved carbon supports for efficient electrocatalytic hydrogen evolution. *Nat. Energy* **2019**, *4* (6), 512−518.

(7) Gu, J.; Hsu, C. S.; Bai, L.; Chen, H. M.; Hu, X. Atomically dispersed Fe(3+) sites catalyze efficient CO_2 electroreduction to CO. *Science* **2019**, *364* (6445), 1091−1094.

(8) Liu, M. M.; Wang, L. L.; Zhao, K. N.; Shi, S. S.; Shao, Q. S.; Zhang, L.; Sun, X. L.; Zhao, Y. F.; Zhang, J. J. Atomically dispersed metal catalysts for the oxygen reduction reaction: synthesis, characterization, reaction mechanisms and electrochemical energy applications. *Energy Environ. Sci.* **2019**, *12* (10), 2890−2923.
(9) Xiao, M.; Zhu, J.; Li, G.; Li, N.; Li, S.; Cano, Z. P.; Ma, L.; Cui, P.; Xu, P.; Jiang, G.; Jin, H.; Wang, S.; Wu, T.; Lu, J.; Yu, A.; Su, D.; Chen, Z. A Single-Atom Iridium Heterogeneous Catalyst in Oxygen Reduction Reaction. *Angew. Chem., Int. Ed.* **2019**, *58* (28), 9640−9645.
(10) Jiang, Z.; Sun, W.; Shang, H.; Chen, W.; Sun, T.; Li, H.; Dong, J.; Zhou, J.; Li, Z.; Wang, Y.; Cao, R.; Sarangi, R.; Yang, Z.; Wang, D.; Zhang, J.; Li, Y. Atomic interface effect of a single atom copper catalyst for enhanced oxygen reduction reactions. *Energy Environ. Sci.* **2019**, *12* (12), 3508−3514.
(11) Yao, Y.; Hu, S.; Chen, W.; Huang, Z.-Q.; Wei, W.; Yao, T.; Liu, R.; Zang, K.; Wang, X.; Wu, G.; Yuan, W.; Yuan, T.; Zhu, B.; Liu, W.; Li, Z.; He, D.; Xue, Z.; Wang, Y.; Zheng, X.; Dong, J.; Chang, C.-R.; Chen, Y.; Hong, X.; Luo, J.; Wei, S.; Li, W.-X.; Strasser, P.; Wu, Y.; Li, Y. Engineering the electronic structure of single atom Ru sites via compressive strain boosts acidic water oxidation electrocatalysis. *Nat. Catal.* **2019**, *2* (4), 304−313.
(12) Lee, B. H.; Park, S.; Kim, M.; Sinha, A. K.; Lee, S. C.; Jung, E.; Chang, W. J.; Lee, K. S.; Kim, J. H.; Cho, S. P.; Kim, H.; Nam, K. T.; Hyeon, T. Reversible and cooperative photoactivation of single-atom Cu/TiO_2 photocatalysts. *Nat. Mater.* **2019**, *18* (6), 620−626.
(13) Zhou, L.; Martirez, J. M. P.; Finzel, J.; Zhang, C.; Swearer, D. F.; Tian, S.; Robatjazi, H.; Lou, M.; Dong, L.; Henderson, L.; Christopher, P.; Carter, E. A.; Nordlander, P.; Halas, N. J. Light-driven methane dry reforming with single atomic site antenna-reactor plasmonic photocatalysts. *Nat. Energy* **2020**, *5* (1), 61−70.
(14) Daelman, N.; Capdevila-Cortada, M.; Lopez, N. Dynamic charge and oxidation state of Pt/CeO_2 single-atom catalysts. *Nat. Mater.* **2019**, *18* (11), 1215−1221.
(15) García-Mota, M.; Vojvodic, A.; Metiu, H.; Man, I. C.; Su, H.-Y.; Rossmeisl, J.; Nørskov, J. K. Tailoring the Activity for Oxygen Evolution Electrocatalysis on Rutile TiO_2(110) by Transition-Metal Substitution. *ChemCatChem* **2011**, *3* (10), 1607−1611.
(16) Zhao, Y.; Yang, K. R.; Wang, Z.; Yan, X.; Cao, S.; Ye, Y.; Dong, Q.; Zhang, X.; Thorne, J. E.; Jin, L.; Materna, K. L.; Trimpalis, A.; Bai, H.; Fakra, S. C.; Zhong, X.; Wang, P.; Pan, X.; Guo, J.; Flytzani-Stephanopoulos, M.; Brudvig, G. W.; Batista, V. S.; Wang, D. Stable iridium dinuclear heterogeneous catalysts supported on metal-oxide substrate for solar water oxidation. *Proc. Natl. Acad. Sci. U. S. A.* **2018**, *115* (12), 2902−2907.
(17) Zhao, Y.; Yan, X.; Yang, K. R.; Cao, S.; Dong, Q.; Thorne, J. E.; Materna, K. L.; Zhu, S.; Pan, X.; Flytzani-Stephanopoulos, M.; Brudvig, G. W.; Batista, V. S.; Wang, D. End-On Bound Iridium Dinuclear Heterogeneous Catalysts on WO_3 for Solar Water Oxidation. *ACS Cent. Sci.* **2018**, *4* (9), 1166−1172.
(18) Zhu, C.; Shi, Q.; Feng, S.; Du, D.; Lin, Y. Single-Atom Catalysts for Electrochemical Water Splitting. *ACS Energy Lett.* **2018**, *3* (7), 1713−1721.
(19) Fei, H.; Dong, J.; Feng, Y.; Allen, C. S.; Wan, C.; Volosskiy, B.; Li, M.; Zhao, Z.; Wang, Y.; Sun, H.; An, P.; Chen, W.; Guo, Z.; Lee, C.; Chen, D.; Shakir, I.; Liu, M.; Hu, T.; Li, Y.; Kirkland, A. I.; Duan, X.; Huang, Y. General synthesis and definitive structural identification of MN_4C_4 single-atom catalysts with tunable electrocatalytic activities. *Nat. Catal.* **2018**, *1* (1), 63−72.
(20) Cao, L.; Luo, Q.; Chen, J.; Wang, L.; Lin, Y.; Wang, H.; Liu, X.; Shen, X.; Zhang, W.; Liu, W.; Qi, Z.; Jiang, Z.; Yang, J.; Yao, T. Dynamic oxygen adsorption on single-atomic Ruthenium catalyst with high performance for acidic oxygen evolution reaction. *Nat. Commun.* **2019**, *10* (1), 4849.
(21) Babic, U.; Suermann, M.; Gubler, L.; Büchi, F. N.; Schmidt, T. J. Identifying critical gaps for polymer electrolyte water electrolysis development. *J. Electrochem. Soc.* **2017**, *164* (4), F387−F399.
(22) Suen, N. T.; Hung, S. F.; Quan, Q.; Zhang, N.; Xu, Y. J.; Chen, H. M. Electrocatalysis for the oxygen evolution reaction: recent development and future perspectives. *Chem. Soc. Rev.* **2017**, *46* (2), 337−365.
(23) Meyer, T. J.; Sheridan, M. V.; Sherman, B. D. Mechanisms of molecular water oxidation in solution and on oxide surfaces. *Chem. Soc. Rev.* **2017**, *46* (20), 6148−6169.
(24) McCrory, C. C.; Jung, S.; Peters, J. C.; Jaramillo, T. F. Benchmarking heterogeneous electrocatalysts for the oxygen evolution reaction. *J. Am. Chem. Soc.* **2013**, *135* (45), 16977−16987.
(25) Ezhov, R.; Karbakhsh Ravari, A.; Page, A.; Pushkar, Y. Water Oxidation Catalyst cis-$[Ru(bpy)(5,5'\text{-dcbpy})(H_2O)_2]^{2+}$ and Its Stabilization in Metal−Organic Framework. *ACS Catal.* **2020**, *10* (9), 5299−5308.
(26) Reier, T.; Nong, H. N.; Teschner, D.; Schlögl, R.; Strasser, P. Electrocatalytic Oxygen Evolution Reaction in Acidic Environments - Reaction Mechanisms and Catalysts. *Adv. Energy Mater.* **2017**, *7* (1), 1601275.
(27) Lebedev, D.; Pineda-Galvan, Y.; Tokimaru, Y.; Fedorov, A.; Kaeffer, N.; Coperet, C.; Pushkar, Y. The Key Ru(V)═O Intermediate of Site-Isolated Mononuclear Water Oxidation Catalyst Detected by in Situ X-ray Absorption Spectroscopy. *J. Am. Chem. Soc.* **2018**, *140* (1), 451−458.
(28) Davis, K. M.; Sullivan, B. T.; Palenik, M. C.; Yan, L.; Purohit, V.; Robison, G.; Kosheleva, I.; Henning, R. W.; Seidler, G. T.; Pushkar, Y. Rapid evolution of the Photosystem II electronic structure during water splitting. *Phys. Rev. X* **2018**, *8* (4), 041014.
(29) Sanchez Casalongue, H. G.; Ng, M. L.; Kaya, S.; Friebel, D.; Ogasawara, H.; Nilsson, A. In situ observation of surface species on iridium oxide nanoparticles during the oxygen evolution reaction. *Angew. Chem., Int. Ed.* **2014**, *53* (28), 7169−7172.
(30) Pedersen, A. F.; Escudero-Escribano, M.; Sebok, B.; Bodin, A.; Paoli, E.; Frydendal, R.; Friebel, D.; Stephens, I. E. L.; Rossmeisl, J.; Chorkendorff, I.; Nilsson, A. Operando XAS Study of the Surface Oxidation State on a Monolayer IrO_x on RuO_x and Ru Oxide Based Nanoparticles for Oxygen Evolution in Acidic Media. *J. Phys. Chem. B* **2018**, *122* (2), 878−887.
(31) Wang, J.; Yin, G.; Shao, Y.; Zhang, S.; Wang, Z.; Gao, Y. Effect of carbon black support corrosion on the durability of Pt/C catalyst. *J. Power Sources* **2007**, *171* (2), 331−339.
(32) Stalzer, M. M.; Delferro, M.; Marks, T. J. Supported Single-Site Organometallic Catalysts for the Synthesis of High-Performance Polyolefins. *Catal. Lett.* **2015**, *145* (1), 3−14.
(33) Pelletier, J. D.; Basset, J. M. Catalysis by Design: Well-Defined Single-Site Heterogeneous Catalysts. *Acc. Chem. Res.* **2016**, *49* (4), 664−677.
(34) Coperet, C.; Comas-Vives, A.; Conley, M. P.; Estes, D. P.; Fedorov, A.; Mougel, V.; Nagae, H.; Nunez-Zarur, F.; Zhizhko, P. A. Surface Organometallic and Coordination Chemistry toward Single-Site Heterogeneous Catalysts: Strategies, Methods, Structures, and Activities. *Chem. Rev.* **2016**, *116* (2), 323−421.
(35) Coperet, C. Single-Sites and Nanoparticles at Tailored Interfaces Prepared via Surface Organometallic Chemistry from Thermolytic Molecular Precursors. *Acc. Chem. Res.* **2019**, *52* (6), 1697−1708.
(36) Copéret, C. Fuels and energy carriers from single-site catalysts prepared via surface organometallic chemistry. *Nat. Energy* **2019**, *4* (12), 1018−1024.
(37) Lebedev, D.; Copéret, C. Small, Narrowly Distributed Iridium Nanoparticles Supported on Indium Tin Oxide for Efficient Anodic Water Oxidation. *ACS Appl. Energy Mater.* **2019**, *2* (1), 196−200.
(38) Oh, H.-S.; Nong, H. N.; Reier, T.; Bergmann, A.; Gliech, M.; Ferreira de Araújo, J.; Willinger, E.; Schlögl, R.; Teschner, D.; Strasser, P. Electrochemical Catalyst-Support Effects and Their Stabilizing Role for IrO_x Nanoparticle Catalysts during the Oxygen Evolution Reaction. *J. Am. Chem. Soc.* **2016**, *138* (38), 12552−12563.
(39) Abbott, D. F.; Lebedev, D.; Waltar, K.; Povia, M.; Nachtegaal, M.; Fabbri, E.; Copéret, C.; Schmidt, T. J. Iridium Oxide for the Oxygen Evolution Reaction: Correlation between Particle Size, Morphology, and the Surface Hydroxo Layer from Operando XAS. *Chem. Mater.* **2016**, *28* (18), 6591−6604.

https://dx.doi.org/10.1021/acscentsci.0c00604
ACS Cent. Sci. 2020, 6, 1189−1198

(40) Pfeifer, V.; Jones, T. E.; Velasco Vélez, J. J.; Massué, C.; Arrigo, R.; Teschner, D.; Girgsdies, F.; Scherzer, M.; Greiner, M. T.; Allan, J.; Hashagen, M.; Weinberg, G.; Piccinin, S.; Hävecker, M.; Knop-Gericke, A.; Schlögl, R. The electronic structure of iridium and its oxides. *Surf. Interface Anal.* **2016**, *48* (5), 261−273.
(41) Lebedev, D.; Povia, M.; Waltar, K.; Abdala, P. M.; Castelli, I. E.; Fabbri, E.; Blanco, M. V.; Fedorov, A.; Copéret, C.; Marzari, N.; Schmidt, T. J. Highly Active and Stable Iridium Pyrochlores for Oxygen Evolution Reaction. *Chem. Mater.* **2017**, *29* (12), 5182−5191.
(42) Lettenmeier, P.; Majchel, J.; Wang, L.; Saveleva, V. A.; Zafeiratos, S.; Savinova, E. R.; Gallet, J. J.; Bournel, F.; Gago, A. S.; Friedrich, K. A. Highly active nano-sized iridium catalysts: synthesis and operando spectroscopy in a proton exchange membrane electrolyzer. *Chem. Sci.* **2018**, *9* (14), 3570−3579.
(43) Fu, L.; Zeng, X.; Huang, C.; Cai, P.; Cheng, G.; Luo, W. Ultrasmall Ir nanoparticles for efficient acidic electrochemical water splitting. *Inorg. Chem. Front.* **2018**, *5* (5), 1121−1125.
(44) Sheehan, S. W.; Thomsen, J. M.; Hintermair, U.; Crabtree, R. H.; Brudvig, G. W.; Schmuttenmaer, C. A. A molecular catalyst for water oxidation that binds to metal oxide surfaces. *Nat. Commun.* **2015**, *6*, 6469.
(45) Oakton, E.; Lebedev, D.; Povia, M.; Abbott, D. F.; Fabbri, E.; Fedorov, A.; Nachtegaal, M.; Copéret, C.; Schmidt, T. J. IrO_2-TiO_2: A High-Surface-Area, Active, and Stable Electrocatalyst for the Oxygen Evolution Reaction. *ACS Catal.* **2017**, *7*, 2346−2352.
(46) Chen, J.; Cui, P.; Zhao, G.; Rui, K.; Lao, M.; Chen, Y.; Zheng, X.; Jiang, Y.; Pan, H.; Dou, S. X.; Sun, W. Low-Coordinate Iridium Oxide Confined on Graphitic Carbon Nitride for Highly Efficient Oxygen Evolution. *Angew. Chem., Int. Ed.* **2019**, *58* (36), 12540−12544.
(47) Nong, H. N.; Reier, T.; Oh, H.-S.; Gliech, M.; Paciok, P.; Vu, T. H. T.; Teschner, D.; Heggen, M.; Petkov, V.; Schlögl, R.; Jones, T.; Strasser, P. A unique oxygen ligand environment facilitates water oxidation in hole-doped $IrNiO_x$ core−shell electrocatalysts. *Nat. Catal.* **2018**, *1* (11), 841−851.
(48) Zheng, T.; Shang, C.; He, Z.; Wang, X.; Cao, C.; Li, H.; Si, R.; Pan, B.; Zhou, S.; Zeng, J. Intercalated Iridium Diselenide Electrocatalysts for Efficient pH-Universal Water Splitting. *Angew. Chem., Int. Ed.* **2019**, *58* (41), 14764−14769.
(49) Hay-Motherwell, R. S.; Wilkinson, G.; Hussain-Bates, B.; Hursthouse, M. B. Synthesis and X-ray crystal structure of oxotrimesityliridium(V). *Polyhedron* **1993**, *12* (16), 2009−2012.
(50) Vilella, L.; Vidossich, P.; Balcells, D.; Lledos, A. Basic ancillary ligands promote O-O bond formation in iridium-catalyzed water oxidation: a DFT study. *Dalton Trans.* **2011**, *40* (42), 11241−11247.
(51) Liao, R.-Z.; Siegbahn, P. E. M. Which Oxidation State Leads to O−O Bond Formation in Cp*Ir(bpy)Cl-Catalyzed Water Oxidation, Ir(V), Ir(VI), or Ir(VII)? *ACS Catal.* **2014**, *4* (11), 3937−3949.
(52) Moonshiram, D.; Alperovich, I.; Concepcion, J. J.; Meyer, T. J.; Pushkar, Y. Experimental demonstration of radicaloid character in a Ru^V=O intermediate in catalytic water oxidation. *Proc. Natl. Acad. Sci. U. S. A.* **2013**, *110* (10), 3765−3770.
(53) Erdman, D.; Pineda-Galvan, Y.; Pushkar, Y. Mechanistic Analysis of Water Oxidation Catalyst cis-$[Ru(bpy)_2(H_2O)_2]^{2+}$: Effect of Dimerization. *Catalysts* **2017**, *7* (2), 39.
(54) Pineda-Galvan, Y.; Ravari, A. K.; Shmakov, S.; Lifshits, L.; Kaveevivitchai, N.; Thummel, R.; Pushkar, Y. Detection of the site protected 7-coordinate Ru^V=O species and its chemical reactivity to enable catalytic water oxidation. *J. Catal.* **2019**, *375*, 1−7.
(55) Truscott, B. J.; Nelson, D. J.; Lujan, C.; Slawin, A. M.; Nolan, S. P. Iridium(I) hydroxides: powerful synthons for bond activation. *Chem. - Eur. J.* **2013**, *19* (24), 7904−7916.
(56) Farnum, B. H.; Morseth, Z. A.; Brennaman, M. K.; Papanikolas, J. M.; Meyer, T. J. Driving force dependent, photoinduced electron transfer at degenerately doped, optically transparent semiconductor nanoparticle interfaces. *J. Am. Chem. Soc.* **2014**, *136* (45), 15869−15872.
(57) Shirley, D. A. High-Resolution X-Ray Photoemission Spectrum of the Valence Bands of Gold. *Phys. Rev. B* **1972**, *5* (12), 4709−4714.
(58) Ravel, B.; Newville, M. ATHENA, ARTEMIS, HEPHAESTUS: data analysis for X-ray absorption spectroscopy using IFEFFIT. *J. Synchrotron Radiat.* **2005**, *12* (4), 537−541.
(59) Perdew, J. P.; Burke, K.; Ernzerhof, M. Generalized Gradient Approximation Made Simple. *Phys. Rev. Lett.* **1996**, *77* (18), 3865−3868.
(60) Grimme, S. Accurate description of van der Waals complexes by density functional theory including empirical corrections. *J. Comput. Chem.* **2004**, *25* (12), 1463−1473.
(61) Kresse, G.; Furthmuller, J. Efficient iterative schemes for ab initio total-energy calculations using a plane-wave basis set. *Phys. Rev. B: Condens. Matter Mater. Phys.* **1996**, *54* (16), 11169−11186.
(62) Kresse, G.; Hafner, J. Ab initio molecular dynamics for liquid metals. *Phys. Rev. B: Condens. Matter Mater. Phys.* **1993**, *47* (1), 558−561.
(63) Svensson, M.; Humbel, S.; Froese, R. D. J.; Matsubara, T.; Sieber, S.; Morokuma, K. ONIOM: A Multilayered Integrated MO + MM Method for Geometry Optimizations and Single Point Energy Predictions. A Test for Diels−Alder Reactions and $Pt(P(t\text{-}Bu)_3)_2$ + H_2 Oxidative Addition. *J. Phys. Chem.* **1996**, *100* (50), 19357−19363.
(64) Karton, A.; Tarnopolsky, A.; Lamere, J. F.; Schatz, G. C.; Martin, J. M. Highly accurate first-principles benchmark data sets for the parametrization and validation of density functional and other approximate methods. Derivation of a robust, generally applicable, double-hybrid functional for thermochemistry and thermochemical kinetics. *J. Phys. Chem. A* **2008**, *112* (50), 12868−12886.
(65) Neese, F. The ORCA program system. *Wiley Interdiscip. Rev.: Comput. Mol. Sci.* **2012**, *2* (1), 73−78.
(66) Weigend, F.; Ahlrichs, R. Balanced basis sets of split valence, triple zeta valence and quadruple zeta valence quality for H to Rn: Design and assessment of accuracy. *Phys. Chem. Chem. Phys.* **2005**, *7* (18), 3297−3305.

https://dx.doi.org/10.1021/acscentsci.0c00604
ACS Cent. Sci. 2020, 6, 1189−1198